Research on Engineering Structures & Materials
www.jresm.org
Research Group

Research Article

A condition-based hybrid model for estimating liquefaction-induced lateral spreading

Engin Nacaroğlu [*,a], Berk Yağcıoğlu [b]

Department of Civil Engineering, Pamukkale University, Engineering Faculty, Türkiye

Article Info

Article History:

Received 18 Mar 2026

Accepted 15 July 2026

Keywords:

Lateral spreading;
Soil liquefaction;
Decision tree algorithm;
Cone Penetration Test;
Hybrid approach

Abstract

In the event of soil liquefaction, the subjection of the ground to topographic elevation differences, such as in free field or gently sloping ground conditions, leads to lateral spreading, which is one of the most severe forms of liquefaction-induced ground deformation. This study investigates the predictive capabilities of the two widely adopted empirical models by Zhang et al. (2004) and Youd et al. (2002) for predicting liquefaction-induced lateral spreading. Utilizing high-resolution aerial LiDAR measurements and 83 Cone Penetration Test (CPT) data from the 2011 Christchurch earthquake, the study identifies significant predictive limitations in both models when applied outside their optimal conditions. The Zhang model often overpredicts steep slopes, while the Youd model tends to under-predict massive displacements in deep, clean sand deposits. To minimize these mispredictions, tiered hybrid model-selection scheme was developed using a Decision Tree machine learning algorithm. This condition-based selection approach uses free face ratio (W), liquefiable layer thickness (T_{15}), and CPT tip resistance (q_c) to alternate between the two methodologies. The findings show that combining the two methods yields better results than using only one method within study limitations.

1. Introduction

In the event of soil liquefaction, the subjection of the ground to topographic elevation differences, such as in free field or gently sloping ground conditions, leads to lateral spreading, which is one of the most severe forms of liquefaction-induced ground deformation. Lateral spreading deformations can cause meters of permanent ground displacement, resulting in extensive damage to both infrastructure [1,2] and superstructure foundations [3]. Lateral spreading has been observed in earthquakes such as the 1999 Chi-Chi earthquake [4], the 1999 Kocaeli earthquake [5], the 2010-2011 Christchurch earthquake sequence [6], and the 2023 Kahramanmaraş earthquakes [7,8]. Among the various types of damage caused by liquefaction, lateral spreading is one of the deformation types responsible for the highest total damage [9]. To estimate the magnitude of lateral spreading and elucidate its underlying mechanisms, various studies are being conducted, including field investigations [10], laboratory experiments [11], empirical prediction models based on case histories [12], as well as analytical and numerical models [13].

Regarding the estimation of lateral spreading displacements, the most widely used methods, if not the primary standard, are empirical prediction equations based on the correlation of regional field tests with deformations measured pre- and post-earthquake using various techniques (e.g., LiDAR, aerial photography) within the liquefied zone. In 1987, Hamada et al. [14] developed the first lateral spreading prediction equation of its kind, which was a function of liquefiable layer thickness and ground slope, by utilizing pre- and post-earthquake aerial imagery. Following the observation of subsequent earthquakes and the identification of additional variables influencing lateral spreading,

*Corresponding author: enacaroglu@pau.edu.tr
[a]orcid.org/0000-0002-0693-6534; [b]orcid.org/0000-0003-3156-2287
DOI: http://dx.doi.org/10.17515/resm2026-1572me0318rs

models such as those proposed by [15] began to be adopted. These methods generally consider three distinct topographical conditions driving lateral spreading: gently sloping ground, free field, and combined effects (Figure 1).

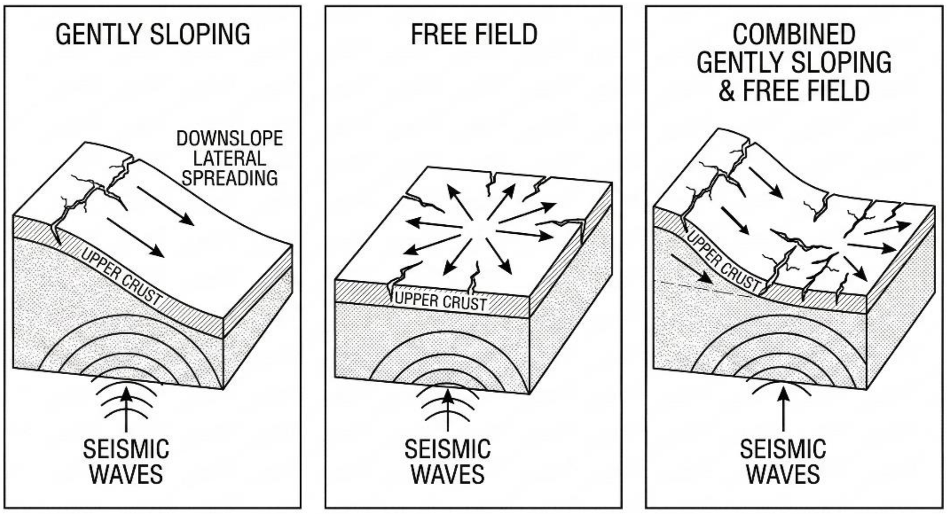

Fig. 1. Schematic illustration of common liquefaction-induced lateral spreading mechanisms: (a) gently sloping ground, (b) free field, and (c) combined conditions (modified from Bartlett and Youd, [12])

Continuous refinement of these frameworks has yielded widely utilized tools, notably the multi-linear regression model by Youd et al. [16] and the strain-integration approach proposed by Zhang et al. [17], which utilizes the Lateral Displacement Index (LDI) derived from CPT data. Existing methods often demonstrate significant predictive limitations when applied outside their optimal boundary conditions. For instance, regression-based models (e.g., Youd et al., [16]) frequently under-predict massive ground displacements in deep liquefiable deposits with mild slopes due to statistical ceiling effects. Conversely, models relying on maximum shear strain integration (e.g., Zhang et al., [17]) tend to yield unrealistic over-predictions in steep topographical conditions or high free-face ratios, where the mathematical boundaries of the equations become unstable. Furthermore, independent validations of the Zhang et al. [17] framework have previously reported highly conservative over-predictions, with estimated displacements exceeding the actual measured values by up to six to eight times [18]. Furthermore, the accuracy of liquefaction and lateral spreading assessments heavily relies on the reliable estimation of seismic demand parameters [19].

Relying exclusively on a single empirical model across diverse and complex site profiles can lead to critical under- or overestimations of expected ground deformation. A condition-based selection approach might be utilized to integrate the specific strengths of distinct models while promisingly preventing or minimizing their specific vulnerabilities for different cases. Accordingly, this study proposes a tiered hybrid prediction framework optimized through decision tree algorithms. By systematically integrating key driving factors, namely, free face ratio (W), liquefiable layer thickness (T_{15}), and CPT tip resistance (q_c), a conditional selection matrix is developed to dynamically alternate between the Youd et al. [16] and Zhang et al. [17] methodologies. The selection of the Youd et al. [16] and Zhang et al. [17] models is justified by their status as widely accepted industry standards, representing two distinct fundamental methodologies—multiple linear regression and CPT-based strain integration, respectively—for predicting liquefaction-induced lateral spreading. The primary objective of this research is to establish a more accurate, site-specific evaluation decision algorithm that mitigates the extreme error margins of individual empirical equations, thereby improving the accuracy and engineering reliability of lateral spreading estimations.

2. Material and Methods

2.1. Data Set Creation

The South Island of New Zealand was subjected to successive severe shaking and thousands of aftershocks during the seismic activity known in the literature as the Canterbury Earthquake Sequence, which began with the Mw 7.1 Darfield earthquake on September 4, 2010. The most destructive phase of this sequence, the Mw 6.2 Christchurch earthquake on February 22, 2011, generated high acceleration values in the region due to its proximity to the city center and shallow focal depth. The resulting severe ground motions triggered widespread liquefaction within the soil profiles in and around Christchurch; particularly, severe lateral spreading in areas adjacent to rivers and free faces caused heavy damage to infrastructure and superstructure systems. To evaluate the methods, 83 Cone Penetration Test (CPT) soundings were selected from the Avon River region in Christchurch (Figure 2).

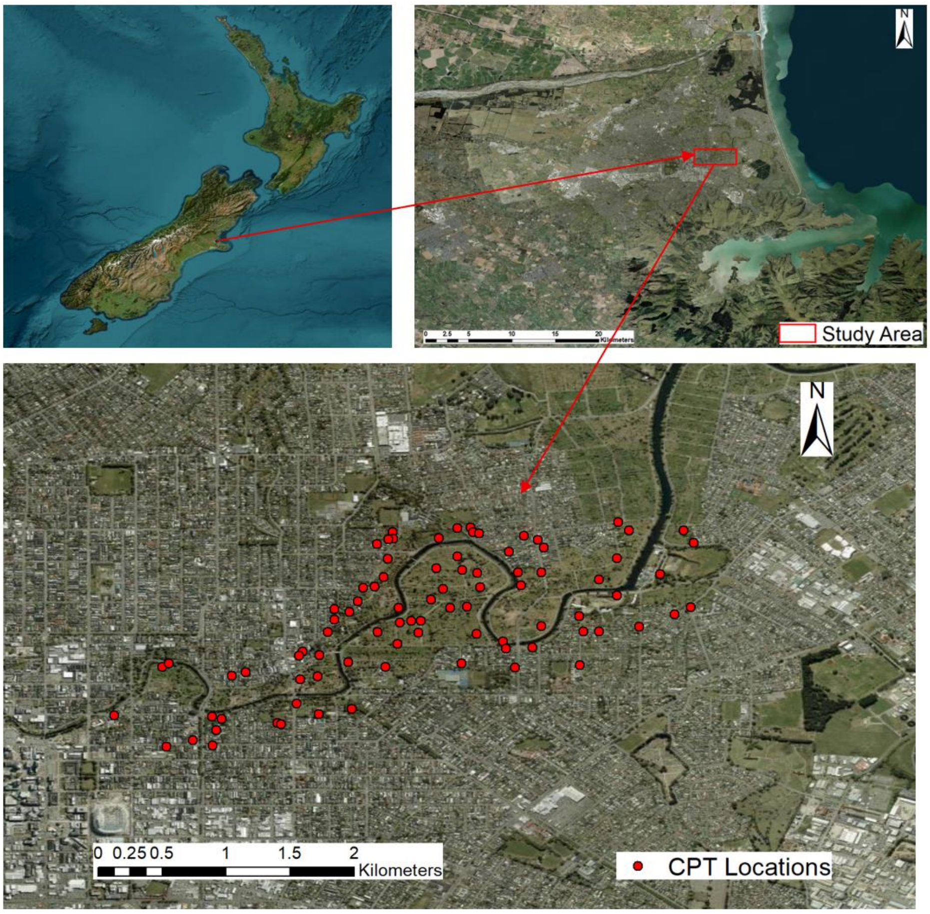

Fig. 2. Location map of the study area within the Avon River region of Christchurch, New Zealand, and the distribution of the selected 83 Cone Penetration Test (CPT) soundings

Table 1. Range of the geotechnical and topographical parameters utilized in the dataset

Data Type	Value Range
Thickness of liquefiable layer (T15)	0 m – 4.88 m
Median grain size of liquefiable layer (D50)	0.04 mm – 1.2 mm
Free-face ratio (%W)	0.73% – 50%
Ground slope (%S)	0.43% – 30%
Average fines content of liquefiable layer (F15)	0% – 24%

The selection of the data aimed to diversify parameters such as the free-face ratio (%W), ground slope, median grain size of the liquefiable layer (D_{50}), and the thickness of the liquefiable layer (T_{15}). The data were obtained from the New Zealand Geotechnical Database (NZGD). The data ranges utilized in the study are presented in Table 1. All selected CPT data extend to a depth of at least 10 meters. For CPT profiles terminating at exactly 10 meters, it has been verified that no liquefiable soil layer exists below this depth.

2.2 Lateral Spreading Prediction Equations

The methods proposed by Youd et al. [16] and Zhang et al. [17] were selected as the lateral spreading prediction models. The prediction equation was established by updating the empirical models previously developed by Bartlett and Youd [12,15] with new earthquake and soil data. In this approach, the prediction equations presented in Equation 1 and Equation 2 were developed through Multiple Linear Regression utilizing soil and seismic data. The variables utilized in the equations include the estimated displacement (D_H), earthquake magnitude (M), modified distance to the fault rupture (R*), free-face ratio (W%), ground slope (S%), median grain size of the liquefiable layer (D_{50}), and thickness of the liquefiable layer (T_{15}).

$$\begin{aligned} log\ D_H = & -16.713 + 1.532M - 1.406 log\ R^* - 0.012R \\ & +0.592 log\ W + 0.540 log\ T_{15} + 3.413 log\,(100 - F_{15}) \\ & -0.795 log\,(D50_{15} + 0.1mm) \end{aligned} \tag{1}$$

$$\begin{aligned} log\ D_H = & -16.213 + 1.532M - 1.406 log\ R^* - 0.012R \\ & +0.338 log\ S + 0.540 log\ T_{15} + 3.413 log\,(100 - F_{15}) \\ & -0.795 log\,(D50_{15} + 0.1mm) \end{aligned} \tag{2}$$

In the model proposed by Zhang et al. [17], the maximum cyclic shear strain is determined based on the relative density derived from SPT or CPT data. The Lateral Displacement Index (LDI) is calculated by multiplying the shear strain by the thickness of the deforming layer. Using the determined LDI value, ground slope (S%), and free-face ratio (L/H), lateral spreading is estimated via the formulas provided in Equation 3, Equation 4, and Equation 5.

$$LD = (S + 0.2) \cdot LDI \tag{3}$$

$$LD = 6 \cdot (L/H)^{-0.8} \cdot LDI \tag{4}$$

$$LDI = \int_0^{Z_{max}} \gamma_{max} dz \tag{5}$$

2.3 Determination of Lateral Spread Parameters Through CPT Data

To classify the soils as liquefiable or non-liquefiable using CPT data, the soil behavior type index (I_c) was determined. I_c was calculated based on the methodology proposed by Robertson and Wride [20] utilizing Equation 6, Equation 7, and Equation 8. Here, Q and F represent the normalized CPT tip resistance and normalized friction ratio, respectively. The stress exponent (n) was determined iteratively as a function of I_c, in accordance with Robertson [21]. Based on the calculated I_c values, soils with an I_c > 2.6 were assumed to exhibit clay-like behavior and were consequently classified as non-liquefiable.

$$I_c = [(3.47 - log\,(Q))^2 + (1.22 + log\,(F))^2]^{0.5} \tag{6}$$

$$Q = \left(\frac{q_c - \sigma_{vc}}{P_a}\right)\left(\frac{P_a}{\sigma'_{vc}}\right)^n \tag{7}$$

$$F = \left(\frac{f_s}{q_c - \sigma_{vc}}\right) \cdot 100\% \tag{8}$$

Using the methodology proposed by Boulanger and Idriss [22], the factors of safety (FS) for the CPT data were determined via Equation 9, Equation 10, and Equation 11.

$$CRR_{M=7.5,\sigma'_v=1atm} = exp\left(\frac{q_{c1Ncs}}{113} + \left(\frac{q_{c1Ncs}}{1000}\right)^2 - \left(\frac{q_{c1Ncs}}{140}\right)^3 + \left(\frac{q_{c1Ncs}}{137}\right)^4 - 2.80\right) \tag{9}$$

$$CSR_{M,\sigma'_v} = 0.65 \frac{\sigma_v}{\sigma'_v} \frac{a_{max}}{g} r_d \tag{10}$$

$$FS = \frac{CRR_{M,\sigma'_v}}{CSR_{M,\sigma'_v}} \tag{11}$$

The liquefiable layer thicknesses were established by summing the thicknesses of all layers where FS < 2 and I_c < 2.6. The distribution of the liquefiable layer thickness dataset is presented in Figure 3.

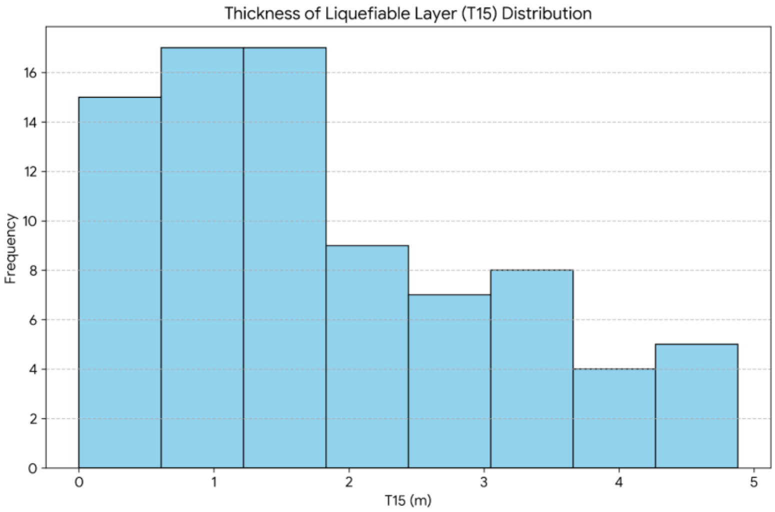

Fig. 3. Histogram illustrates the frequency distribution of the liquefiable layer thickness (T_{15}) for the evaluated CPT soundings

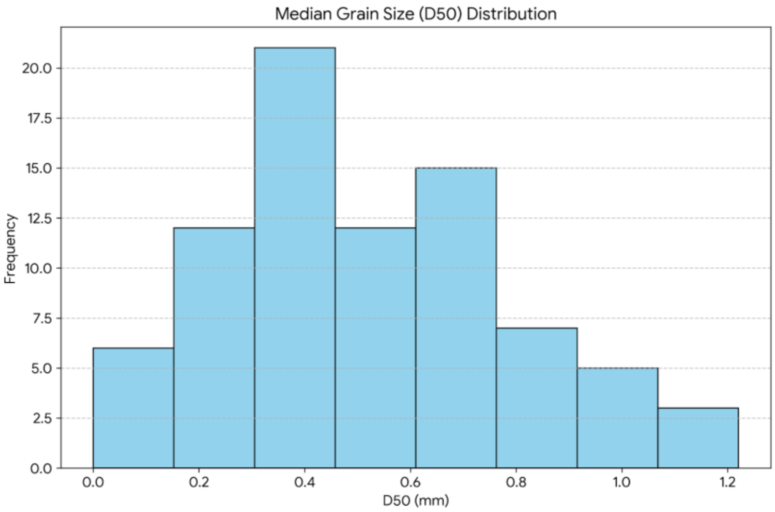

Fig. 4. Frequency distribution of the median grain size (D_{50}) within the identified liquefiable layers of the dataset

For the identified liquefiable layers, the median grain size (D_{50}) was determined using the soil behavior type index (I_c). For this process, a regression analysis was performed on the I_c and corresponding D_{50} values in Table 2 to formulate an equation relating to I_c and D_{50} (Equation 12). The distribution of the liquefiable layer median grain size dataset is presented in Figure 4. The average fines content of the liquefiable layer (F_{15}) was determined according to Boulanger and Idriss [21] (Equation 13). The distribution of the liquefiable layer fine content size dataset is presented in Figure 5.

$$D_{50} = 10^{(2.194 - 1.247 * I_c)} \tag{12}$$

$$FC = 80(I_C + C_{FC}) - 137 \tag{13}$$

Table 2. Soil behavior type index (I_c) boundaries and corresponding median grain size (D_{50}) estimations.

Soil Type	Boundary Ic	Boundary D50
Gravel Boundary	1.31	3.65 mm
Clean Sand Boundary	2.05	0.43 mm
Silt Boundary	2.6	0.09 mm

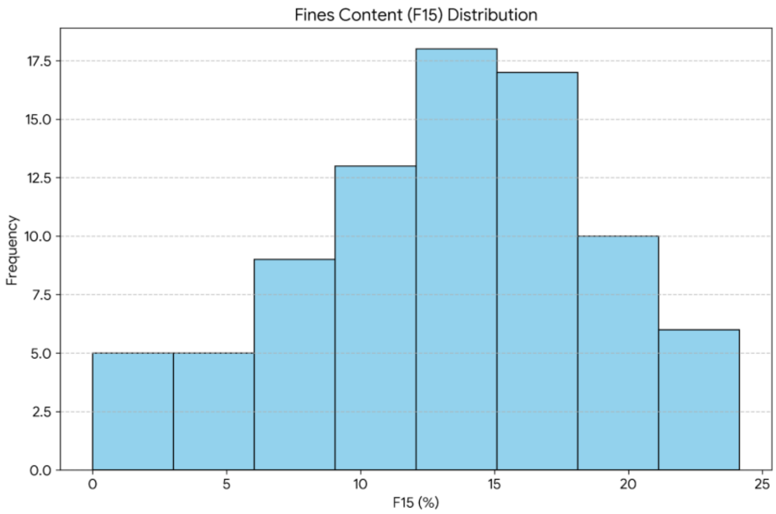

Fig. 5. Histogram depicting the distribution of the average fines content (F_{15}) for the analyzed liquefiable profiles

To accurately evaluate the effects of liquefaction-induced lateral spreading and ground deformations that occurred during the 2011 Christchurch earthquake, high-resolution aerial LiDAR (Light Detection and Ranging) measurements were utilized. Pre- and post-earthquake LiDAR datasets were analyzed using sub-pixel correlation techniques to map horizontal ground displacements and areal strains [23]. These measurements provide accuracy ranging from 40-55 cm horizontally, and ±7 to ±15 cm vertically [24]. As emphasized by the study conducted by Robinson [25], although local ground surveys and local crack measurements provide detailed data, they can be insufficient in fully capturing the global movement trends of deformations shaped by topographic effects. At this point, LiDAR data plays a critical complementary role to local measurements by clearly revealing the macro-scale movement patterns of lateral spreading. This high-resolution and holistic lateral ground deformation data obtained via LiDAR (e.g., analyses conducted with 4-meter spatial resolutions instead of 56-meter) [26] has played a crucial role in the seismic damage assessments of buried pipelines and infrastructure systems in liquefied zones by capturing local deformation variations in detail. The average depth of the Avon River was used as the free field height, which is 2.5 meters. The free surface distance distributions are shown in Figure 6. Using Tatsuoka et al. [27], relative density values were determined for each CPT thickness (Equation 14). Maximum cyclic shear strain values γ_{max} (%) were determined based on D_r and FS.

$$D_r = -85 + 76\,log(q_{c1N}) \qquad (q_{c1N} \leqslant 200) \tag{14}$$

Upon evaluating the liquefaction triggering potential across the initial dataset, it was determined that 6 out of the 83 selected CPT soundings did not exhibit any liquefaction ($T_{15} \approx 0$). Since the empirical lateral spreading models evaluated in this study are strictly applicable to liquefied soils, including non-liquefying sites—where measured surface deformations are likely driven by other geological or non-seismic factors—artificially skew the error metrics of the models. Consequently, these 6 soundings were excluded from the analysis.

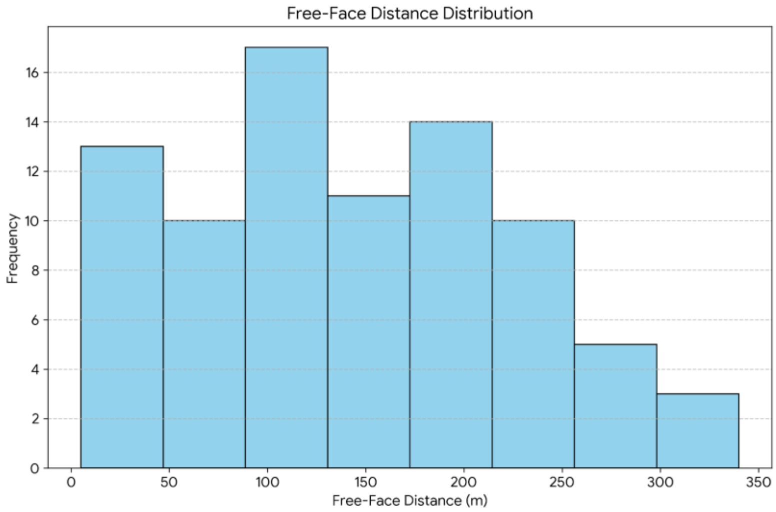

Figure 6. Distribution of the free-face distance (L) for the selected CPT locations adjacent to the Avon River

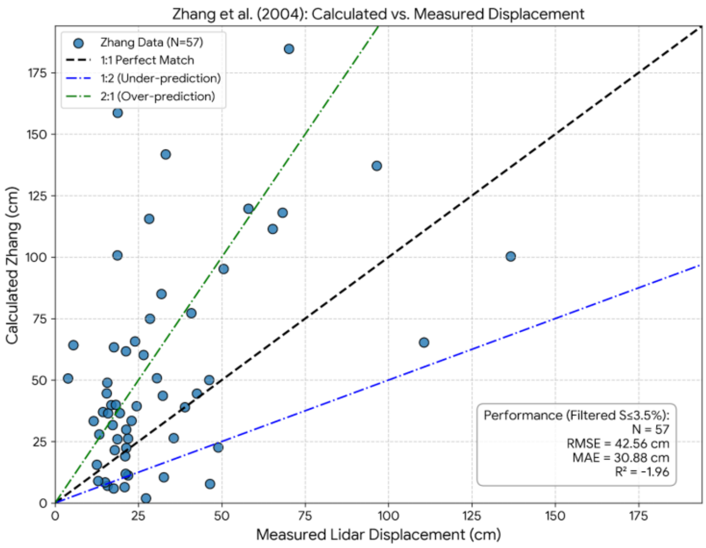

Fig. 7. Comparison of measured LiDAR displacements versus lateral spreading predictions calculated by the Zhang et al. [17] model for filtered data points (S ≤ 3.5%, N=57)

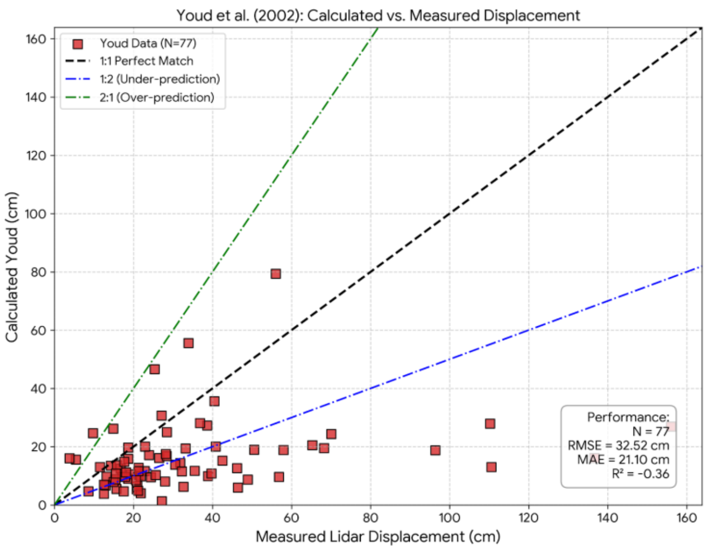

Fig. 8. Comparison of measured LiDAR displacements versus lateral spreading predictions calculated by the Youd et al. [16] model for the entire dataset (N=77)

All subsequent predictive modeling, error analyses, and decision tree optimizations were conducted on the refined final dataset consisting of 77 valid liquefaction points. The lateral spread displacements calculated and measured for Zhang et al. [17] for 57 data points are shown in Figure 7, and 77 data for Youd et al. [16] are shown in Figure 8. Only data where $S < 3.5$ were used (as method suggest) for the Zhang model; data not meeting this condition yielded highly unrelated results, so the number of data points for the Zhang model decreased from 83 to 57.

2.4 Decision Tree Algorithm and Model Architecture

Within the scope of this study, the predictive capabilities of the widely accepted Zhang et al. [17] and Youd et al. [16] models for lateral spreading prediction were tested across the entire dataset (77 CPT). The error analysis (RMSE, MAE) and correlation (R^2) evaluations revealed that both models struggled to fully capture the lateral spreading characteristics, yet their error tendencies were completely distinct from each other. When examining the performance of the Zhang model over the entire dataset, the R^2 value was found to be highly negative (-16.46) and the Root Mean Square Error (RMSE) was significantly high (116.33). The model exhibited mathematical instability, particularly in regions where the free-face ratio (W%) exceeded 3.5% (beyond the recommended applicability bounds for the models, as expected) or the liquefiable layer thickness (T_{15}) was greater than 3 meters. Certain deformations measured between 10-40 cm in the actual field were calculated by the model at astronomically high levels, such as 800 cm to 3000 cm, which are incompatible with physical reality. This indicates that the strain integration approach based on the Lateral Displacement Index (LDI) overreacts at the extreme boundaries of the dataset (especially on steep slopes as method itself mentions).

The most prominent deficiency of the Youd model in this dataset is its tendency to under-predict. Robinson [23] noted that the Youd et al. [16] model frequently under-predicted significant displacements, partially due to the strong magnitude scaling effect restricting the output for the M_w 6.2 event. At critical locations where large lateral spreading of 100-150 cm was observed in the field, the model's predictions remained constrained within the 15-30 cm band. The model failed to capture the site conditions that trigger large displacements. Parametric investigations revealed that the error margin of the Youd model increased in clean sands (fines content, $F_{15} < 10\%$), whereas it yielded results much closer to reality in silty and dirty sands ($F_{15} > 15\%$). Data points where the Zhang and Youd models made their most accurate predictions, it becomes evident that these two models can be used complementarily for different soil and topographic conditions, rather than being direct alternatives to one another. The regions where the models exhibited optimal performance reveal the varying weights they assign to lateral spreading mechanisms.

Upon evaluating results, it was observed that the models' responses to the thickness of the liquefied layer were inversely related. The Zhang model could achieve excellent error margins of 0-4 cm only when the liquefiable layer was thin ($T_{15} < 1.5$ m, average 0.88 m). As the thickness increased, the model's error grew cumulatively. In contrast, the Youd model successfully maintained the error within the 1-3 cm band even in much deeper liquefaction profiles with thicknesses ranging from 2.0 to 3.6 meters. This demonstrates that the regression coefficients in the Youd model more realistically simulate displacement attenuation in thick layers. Almost all the data where the Youd model operated with the lowest error belong to silty and dirty sands with high fines content ($F_{15} > 15\%$). While the Youd model struggled to predict sudden and massive displacements in clean sands, it successfully captured the more viscous and slower-developing lateral spreading characteristics of silty soils. Conversely, the Zhang model provided a more flexible operating range regardless of soil type, provided that the thin-layer condition was satisfied.

For topography, at the locations where it performed nearly perfectly, the Zhang model required topographically gentle slopes with a free-face ratio (W%) ranging between 1% and 3%. As the slope or free-face ratio increased, the model entered geometric instability. On the other hand, the Youd model was able to provide highly accurate results (with a 1-3 cm error margin) even on steep slopes and riverbanks with significantly high free-face ratios, such as 10-12%. Within the scope of this study, a Decision Tree machine learning algorithm was utilized to autonomously select the most appropriate empirical model [16,17] for lateral spreading predictions based on site-specific soil and topographical conditions.

The condition-based selection framework was developed using the CART (Classification and Regression Trees) algorithm. To prevent overfitting on the limited dataset (N=77) and ensure physical geotechnical applicability, hyperparameter tuning was conducted via a Grid Search approach. The investigated hyperparameter space included the maximum tree depth (max depth ranging from 2 to 5) and the minimum number of samples required at a leaf node (minimum samples leaf ranging from 3 to 10). The optimized hyperparameters that minimized the cross-validation error while preserving logical soil mechanics boundaries were finalized as max depth = 3 and minimum samples leaf = 5. At the end, final tree architecture is interpretable, consisting of exactly 11 nodes in total (5 internal splitting nodes and 6 terminal leaves). Based on the mean decrease in Gini impurity, the feature parameter importance (decision weight) of the algorithm was objectively quantified: Free-Face Ratio (W) emerged as the dominant splitting criterion at 48%, followed by the Liquefiable Layer Thickness (T_{15}) at 32%, and the Average Cone Tip Resistance (q_c) at 20%.

Given the restricted size of the eligible liquefaction dataset (N=77), partitioning the data into conventional, static training and testing subsets was deemed unfeasible, as it would risk omitting critical extreme topographical conditions from the learning phase. To rigorously evaluate the model's out of sample predictive performance and explicitly prevent overfitting, a Leave-One-Out Cross-Validation (LOOCV) strategy was implemented. In this validation, the decision tree algorithm was iteratively trained on N-1 (76) samples and tested on the single excluded sample. This process was repeated 77 times for each excluded sample, ensuring that every individual data point served as an unseen test case exactly once. While the training RMSE of the optimized hybrid model was 29.66 cm, the rigorous LOOCV procedure resulted in an out-of-sample validation RMSE of 32.52 cm.

This algorithm (Table 3 and Figure 9) operates on the principle of partitioning each borehole data point in the dataset into homogeneous subgroups (nodes) by testing independent variables such as free face ratio (W), liquefiable layer thickness (T_{15}), and average cone tip resistance (q_c) against mathematical threshold values. During the determination of these thresholds (e.g., W = 1.5% or q_c = 4.0 MPa), the absolute prediction errors generated by the respective models were compared, and the optimal branching rules yielding the highest accuracy were computed by minimizing the Gini Impurity metric. To prevent the model from overfitting the existing dataset and to avoid generating rules that contradict engineering logic, hyperparameter constraints, such as maximum tree depth and minimum leaf samples, were applied to the algorithm. Through the sequential evaluation of various parameter combinations (grid search), a tiered hybrid decision matrix was established. This matrix effectively filters out the blind spots where individual models tend to over-predict or under-predict, thereby simulating the actual field deformation behavior with the lowest possible margin of error.

Table 3. Proposed tiered hybrid decision matrix for lateral spreading prediction model selection.

Free-Face Ratio (W)	Liquefiable Thickness (T15)	Cone Tip Resistance (qc)	Selected Model
Low (W < %1.5)	< 3.0 m	No Effect	Zhang et al. [17]
Low (W < %1.5)	3.0 - 5.0 m	> 4.0 MPa	Zhang et al. [17]
Medium (%1.5 ≤ W < %3.5)	< 1.5 m	No Effect	Zhang et al. [17]
Other	Other	≤ 4.0 MPa	Youd et al. [16]

The free-face ratio limits (W = 1.5% and 3.5%) demarcate the geomorphological transition from gently sloping ground to steep riverbanks; at higher ratios (W > 3.5%), the geometric multipliers in the strain-integration model by Zhang et al. become mathematically unstable and prone to over-prediction, whereas the empirical model by Youd et al. provides more reliable predictions for massive, unconstrained block failures. Furthermore, the cone tip resistance threshold (q_c = 4.0 MPa) represents the approximately very loose sands. For these looser states, the Youd et al. model proves more stable; although it does not utilize q_c or SPT-N values as direct inputs, it effectively accounts for the soil's strength, contractive tendencies, and residual shear resistance through comprehensive index properties, specifically the median grain size (D_{50}) and average fines content

(F_{15}), utilizing them as robust geotechnical proxies within its multilinear regression framework. The T_{15} = 1.5 m threshold distinguishes thin liquefiable layers from deep deposits. In thin layers T_{15} < 1.5 m), Zhang et al.'s model is preferred because it accurately calculates movement based on predictable soil strain. For thicker layers, ground movement involves more complex interactions that are better captured by the broader empirical regression of Youd et al.Decision Tree machine learning algorithm results are shown in Figure 10.

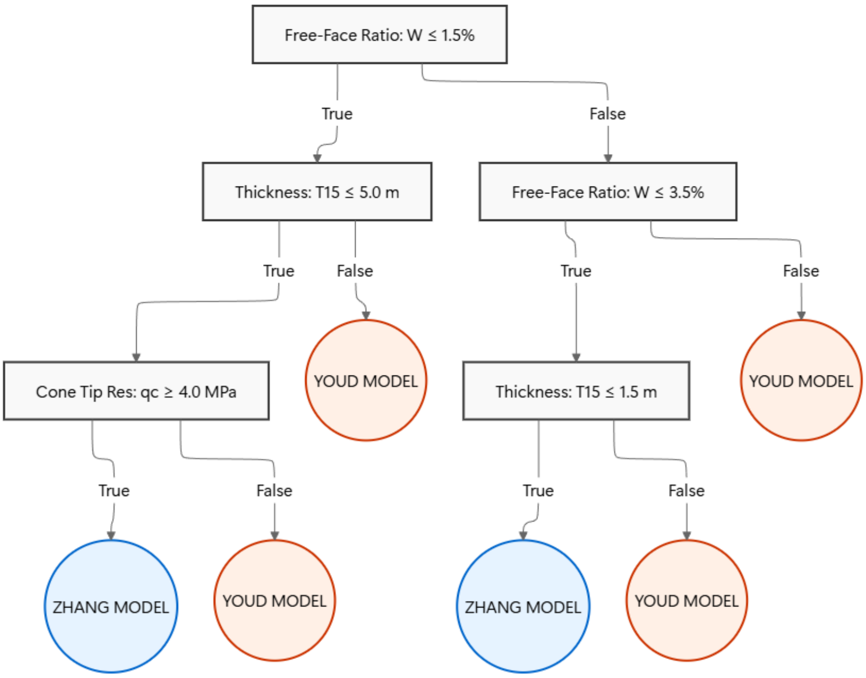

Fig. 9. Proposed tiered hybrid decision frame for lateral spreading prediction model selection

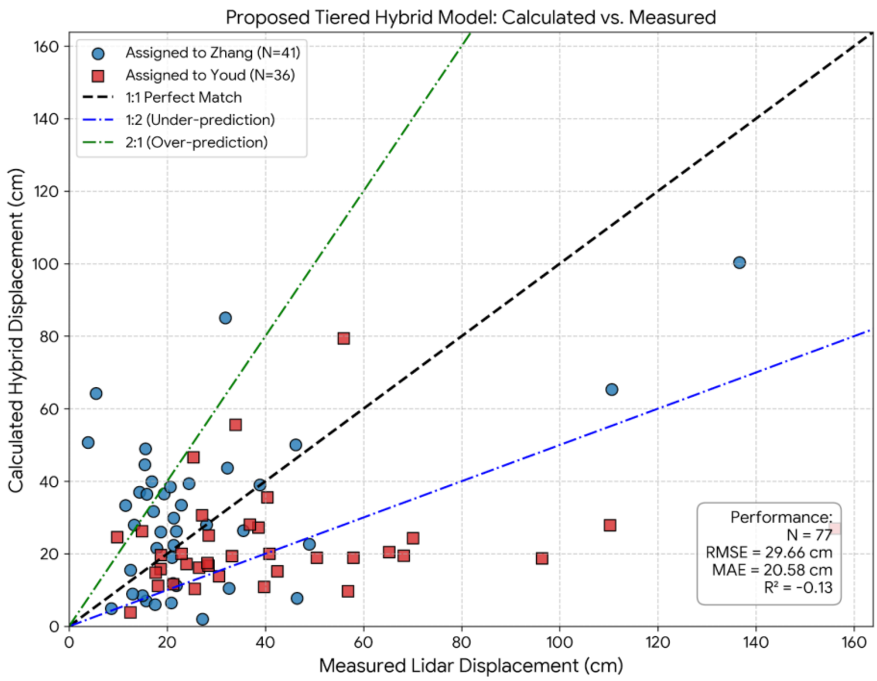

Figure 10. Predictive performance of the Proposed Tiered Hybrid Model comparing calculated versus measured lateral spreading displacements (N=77)

3. Results and Discussion

As presented in Table 4, when evaluated across the entire dataset of 77 valid liquefaction points, the Zhang et al. [17] model exhibits severe instability (RMSE: 116.33 cm), primarily due to its mathematical sensitivity to steep topographical conditions. When 20 high-risk points (S > %3.5) are filtered out and discarded from the dataset, the Zhang model's error is significantly reduced to 42.56 cm. However, discarding nearly 25% of the measured field data is not a practical engineering solution for comprehensive hazard assessment. On the other hand, while the Youd et al. [16] model manages to process the entire dataset without failure, it remains restricted by a steady error margin (RMSE: 32.52 cm) due to its tendency to under-predict massive lateral spreading events. This proposed algorithm reduces the overall RMSE below the 30 cm threshold (29.66 cm) and pushes the R^2 value closer to zero (-0.13), performing better than both isolated models and providing more stable, prediction framework (Table 4).

Table 4. Performance comparison of the isolated empirical equations and the proposed tiered hybrid model

Model / Approach	Data Count (N)	R2 (Coefficient of Determination)	RMSE (Root Mean Square Error)	MAE (cm)	Bias / ME (cm)
Zhang et al. [17] - All Data	77	-16.46	116.33 cm	64.25	+56.09
Zhang et al. [17] - Filtered (S ≤ %3.5)	57	-1.96	42.56 cm	30.88	+21.40
Youd et al. [16] - All Data	77	-0.36	32.52 cm	21.10	-17.97
Proposed Tiered Hybrid Model	77	-0.13	29.66 cm	20.58	-6.57

(Note: Bias/Mean Error (ME) is calculated as Predicted - Measured. A positive ME indicates systemic over-prediction, while a negative ME denotes under-prediction.).

Given the limited size of the dataset (N=77), employing standard machine learning validation techniques such as K-Fold Cross Validation results in unstable decision trees that are overly sensitive to extreme topographical outliers in the test folds. Therefore, the decision tree algorithm was utilized primarily as an exploratory diagnostic tool to identify physically meaningful thresholds (W, T_{15}, q_c) rather than a standalone predictive model. To validate that the proposed model (Table 3) does not suffer from overfitting and provides stable predictions, a Threshold Sensitivity Analysis was conducted (Table 5). The baseline prediction error (RMSE = 29.66 cm) was re-evaluated by systematically varying the critical decision boundaries by ±20%. As demonstrated in the sensitivity results, minor fluctuations in the determined threshold parameters (e.g., altering the W boundary from 1.5% to 2.0% or the q_c threshold from 4.0 MPa to 3.5 MPa) strictly maintains the model's RMSE between 29.87 cm and 33.00 cm. This suggests that the proposed matrix is not excessively sensitive to modest threshold perturbations.

Table 5. Threshold sensitivity analysis of the proposed tiered hybrid framework

Parameter Altered	Baseline Threshold	Tested Threshold	Resulting RMSE
Baseline Model	-	-	29.66 cm
qc (Cone Tip Res.)	4.0 MPa	3.5 MPa	30.15 cm
qc (Cone Tip Res.)	4.0 MPa	4.5 MPa	29.66 cm
T15 (Thickness)	1.5 m	1.0 m	29.87 cm
T15 (Thickness)	1.5 m	2.0 m	29.93 cm
W (Free-Face Ratio)	1.5 %	1.0 %	32.37 cm
W (Free-Face Ratio)	1.5 %	2.0 %	33.00 cm

In the optimization of the decision tree framework, both ground slope (S) and free-face ratio (W) were initially evaluated as potential splitting criteria. However, because the utilized dataset is heavily dominated by the Avon River topography, the lateral spreading mechanism is predominantly governed by the free-face effect rather than the mild general ground slope.

Introducing ground slope ratio as a separate splitting node alongside free face ratio redundantly increased the dimensionality of the model without yielding any predictive gain. the principle of parsimony, the final decision tree was restricted to the most dominant topographical driver (W) combined with geotechnical factors (T_{15}, q_c), resulting in the most robust and physically meaningful architecture.

Table 6. Comprehensive summary matrix

Empirical Model	Optimal Performing Conditions	Weaknesses
Zhang et al. (2004)	Highly accurate for specific bounded topographies: low free-face ratios, thin liquefiable layers and denser sand seams	Prone to severe mathematical instability and catastrophic over-predictions (errors exceeding 400 cm) near unconfined topographical boundaries
Youd et al. (2002)	Highly robust and stable in extreme risk zones high free-face ratios, thick liquefiable layers and denser sand seams	Exhibits statistical ceiling effects, leading to a tendency to under-predict massive lateral spreading displacements.
Proposed Tiered Hybrid	Dynamically adapts to site-specific conditions, successfully neutralizing systemic biases while strictly preventing catastrophic over-predictions.	Accepts under-predictions to completely avoid the risk of massive over-predictions.

While the proposed tiered hybrid model improves the accuracy of lateral spreading predictions, certain limitations of the study should be acknowledged. First, the dataset relies entirely on high-resolution field data obtained from the 2011 Christchurch earthquake. Consequently, the earthquake moment magnitude (M_w) and diverse seismic demand variations were not incorporated as dynamic splitting variables within the decision tree algorithm, as the seismic event was constant across the study area. Second, due to the limited number of eligible liquefaction cases (N=77) encompassing extreme topographical and geotechnical variations, the entire dataset was utilized for algorithmic optimization and model development. Partitioning the data into separate training and testing subsets was not feasible without compromising the statistical representation of critical boundary conditions (e.g., extraordinarily steep slopes or massive displacements). Therefore, while the developed conditional matrix optimizes predictions for the investigated region, future studies incorporating independent, global datasets with varying earthquake magnitudes and diverse geological settings are recommended to validate and further generalize this hybrid framework.

As shown in Figure 10, the hybrid model successfully prevents massive over-predictions. However, this creates a necessary trade-off. In dataset, 14 points (~18%) were assigned to the Youd model, resulting in under-predictions, even though the Zhang model would have been more accurate for those specific points. While the tiered hybrid framework effectively narrows the gap between predicted and observed displacements, the decision tree architecture retains internal constraints. Enhancing the model's robustness through dataset expansion, diversification of input variables, and the application of weighted decision-making is anticipated to significantly improve overall performance metrics. Table 6 provides a summary of the models' performance.

4. Conclusions

Based on the evaluation of lateral spreading prediction models utilizing CPT and high-resolution LiDAR data from the 2011 Christchurch earthquake, the following conclusions are drawn:

- The empirical models proposed by Zhang et al. [17] and Youd et al. [16] exhibit distinct and contrasting error tendencies, indicating that they function better as complementary tools rather than direct alternatives.

- The strain-integration approach of the Zhang et al. [17] demonstrates severe mathematical instability in regions with high free-face ratios (W > 3.5%) or thick liquefiable layers (T_{15} > 3m), leading to unrealistic over-predictions. However, it achieves excellent accuracy for thin liquefiable layers (T_{15} < 1.5 m) on gentle slopes.
- The regression-based Youd et al. [16] model's primary deficiency is its tendency to under-predict massive ground displacements, particularly in clean sands. Conversely, it successfully captures displacement attenuation in thick layers and provides highly accurate results for silty soils and steep slopes.
- A Decision Tree machine learning algorithm optimized a selection model to alternate between the models based on free-face ratio (W), liquefiable layer thickness (T_{15}), and average cone tip resistance (q_c).
- The proposed Tiered Hybrid Model allocates the Zhang model for low free-face ratios (W < 1.5%) up to 5.0 m thickness if the soil is relatively dense (q_c > 4.0 MPa), and for medium free-face ratios (1.5% ≤ W < 3.5%) strictly for thin layers (T_{15} < 1.5 m). The Youd model is designated for all other high-risk conditions.
- By systematically mitigating the extreme prediction errors (blind spots) of the individual empirical equations, the hybrid framework reduced the overall Root Mean Square Error (RMSE) to 29.66 cm and to a certain extent neutralized the systemic bias (Mean Error = -6.57 cm) across the 77 valid data points. While future validation with diverse global datasets is recommended, the proposed condition-based approach yields a modest but consistent improvement for the investigated dataset, providing a more balanced and reliable estimation of lateral spreading hazards.
- Although the results suggest an improved prediction regarding lateral spread estimation, the use of a single earthquake in the study, the fact that the study data was generated for lateral spread under free field (S) effects, and the model data was obtained from a region-specific dataset of 77 points from a single earthquake event indicate that the results are highly open to improvement. Therefore, repeating the study framework with an improved dataset will yield a more generally applicable method.

References

[1] Uckan E, Aksel M, Atas O, Toprak S, Kaya ES. The performance of transmission pipelines on February 6th, 2023 Kahramanmaras earthquake: a series of case studies. Bulletin of Earthquake Engineering. 2025;23(3):1203-1222. https://doi.org/10.1007/s10518-024-01957-2

[2] Toprak S, Wham BP, Nacaroglu E, Ceylan M, Dal O. Performance of water systems during the February 6th Kahramanmaras earthquakes. Earthquake Spectra. 2025;41(1):322-353. https://doi.org/10.1177/87552930241293571

[3] Ozener P, Monkul MM, Eseller Bayat E, Ari A, Cetin KO. Liquefaction and performance of foundation systems in Iskenderun during 2023 Kahramanmaras-Turkiye earthquake sequence. Soil Dynamics and Earthquake Engineering. 2024;178:108433. https://doi.org/10.1016/j.soildyn.2023.108433

[4] Chu DB, Stewart JP, Youd TL, Chu BL. Liquefaction-Induced Lateral Spreading in Near-Fault Regions during the 1999 Chi-Chi, Taiwan Earthquake. Journal of Geotechnical and Geoenvironmental Engineering. 2006;132(12):1549-1565. https://doi.org/10.1061/(ASCE)1090-0241(2006)132:12(1549)

[5] Cetin KO, Youd TL, Seed RB, Bray JD, Stewart JP, Durgunoglu HT, Lettis W, Yilmaz MT. Liquefaction-Induced Lateral Spreading at Izmit Bay During the Kocaeli (Izmit)-Turkey Earthquake. Journal of Geotechnical and Geoenvironmental Engineering. 2004;130(12):1300-1313. https://doi.org/10.1061/(ASCE)1090-0241(2004)130:12(1300)

[6] Cubrinovski M, Robinson K, Taylor M, Hughes M, Orense R. Lateral spreading and its impacts in urban areas in the 2010–2011 Christchurch earthquakes. New Zealand Journal of Geology and Geophysics. 2012;55(3):255-269. https://doi.org/10.1080/00288306.2012.699895

[7] Bol E, Özocak A, Sert S, Çetin KÖ, Arslan E, Kocaman K, Ayhan BU. Evaluation of soil liquefaction in the city of Hatay triggered after the February 6, 2023 Kahramanmaraş-Türkiye earthquake sequence. Engineering Geology. 2024;339:107648. https://doi.org/10.1016/j.enggeo.2024.107648

[8] Toprak S, Zulfikar AC, Mutlu A, Tugsal UM, Nacaroglu E, Karabulut S, Ceylan M, Ozdemir K, Parlak S, Dal O, Karimzadeh S. The aftermath of 2023 Kahramanmaras earthquakes: evaluation of strong motion data, geotechnical, building, and infrastructure issues. Natural Hazards. 2025;121(2):2155-2192. https://doi.org/10.1007/s11069-024-06890-w

[9] National Research Council (NRC). Liquefaction of soils during earthquakes. 1985, Report PB86-163110. Washington, DC: National Academy Press
[10] Zeybek A, Yıldız Ö, Sönmezer YB. Post-earthquake assessment of liquefaction in Gölbaşı-Adıyaman following the 6 February 2023 Kahramanmaraş earthquakes: field observations, SPT-based analysis, and laboratory testing of soil ejecta. Natural Hazards. 2025;121(20):24157-24206. https://doi.org/10.1007/s11069-025-07715-0
[11] Dobry R, Thevanayagam S, Medina C, Bethapudi R, Elgamal A, Bennett V, Abdoun T, Zeghal M, El Shamy U, Mercado VM. Mechanics of Lateral Spreading Observed in a Full-Scale Shake Test. Journal of Geotechnical and Geoenvironmental Engineering. 2011;137(2):115-129. https://doi.org/10.1061/(ASCE)GT.1943-5606.0000409
[12] Bartlett SF, Youd TL. Empirical Prediction of Liquefaction-Induced Lateral Spread. Journal of Geotechnical Engineering. 1995;121(4):316-329. https://doi.org/10.1061/(ASCE)0733-9410(1995)121:4(316)
[13] Ziotopoulou K, Boulanger RW. Plasticity modeling of liquefaction effects under sloping ground and irregular cyclic loading conditions. Soil Dynamics and Earthquake Engineering. 2016;84:269-283. https://doi.org/10.1016/j.soildyn.2016.02.013
[14] Hamada M, Yasuda S, Isoyama R, Emoto K. Study on liquefaction-induced permanent ground displacements and earthquake damage. Doboku Gakkai Ronbunshu. 1986;1986(376):221-229. https://doi.org/10.2208/jscej.1986.376_221
[15] Bartlett SF, Youd TL. Empirical analysis of horizontal ground displacement generated by liquefaction-induced lateral spread. 1992, Technical Report NCEER-92-0021. Buffalo, NY: National Center for Earthquake Engineering Research.
[16] Youd TL, Hansen CM, Bartlett SF. Revised Multilinear Regression Equations for Prediction of Lateral Spread Displacement. Journal of Geotechnical and Geoenvironmental Engineering. 2002;128(12):1007-1017. https://doi.org/10.1061/(ASCE)1090-0241(2002)128:12(1007)
[17] Zhang G, Robertson PK, Brachman RWI. Estimating Liquefaction-Induced Lateral Displacements Using the Standard Penetration Test or Cone Penetration Test. Journal of Geotechnical and Geoenvironmental Engineering. 2004;130(8):861-871. https://doi.org/10.1061/(ASCE)1090-0241(2004)130:8(861)
[18] Araujo W, Ledezma C. Factors That Affect Liquefaction-Induced Lateral Spreading in Large Subduction Earthquakes. Applied Sciences. 2020; 10(18):6503. https://doi.org/10.3390/app10186503
[19] Rouabeh A, Aouari I, Benahmed B, Palanci M. Improved PGA and PGV estimation in soft soils for earthquake engineering applications. Research on Engineering Structures & Materials, 2025. http://doi.org/10.17515/resm2025-857ea0429rs
[20] Robertson PK, Wride CE. Evaluating cyclic liquefaction potential using the cone penetration test. Canadian Geotechnical Journal. 1998;35(3):442-459. https://doi.org/10.1139/t98-017
[21] Robertson PK. Interpretation of cone penetration tests — a unified approach. Canadian Geotechnical Journal. 2009;46(11):1337-1355. https://doi.org/10.1139/T09-065
[22] Boulanger RW, Idriss IM. CPT and SPT based liquefaction triggering procedures. Report No. UCD/CGM-14/01. Davis, CA: Center for Geotechnical Modeling, University of California; 2014.
[23] Beavan J, Motagh M, Fielding EJ, Donnelly N, Collett D. Fault slip models of the 2010–2011 Canterbury, New Zealand, earthquakes from geodetic data and observations of postseismic ground deformation. New Zealand Journal of Geology and Geophysics. 2012;55(3):207-221. https://doi.org/10.1080/00288306.2012.697472
[24] Bouziou D, O'Rourke TD. Response of the Christchurch water distribution system to the 22 February 2011 earthquake. Soil Dynamics and Earthquake Engineering. 2017;97:14-24. https://doi.org/10.1016/j.soildyn.2017.01.035
[25] Robinson K. Liquefaction-induced lateral spreading in the 2010-2011 Canterbury earthquakes, MSc. Thesis, University of Canterbury, Christchurch, New Zealand, 2016.
[26] Toprak S, Nacaroglu E, Koc AC, O'Rourke TD, Hamada M, Cubrinovski M, Van Ballegooy S. Comparison of horizontal ground displacements in Avonside area, Christchurch from air photo, LiDAR and satellite measurements regarding pipeline damage assessment. Bulletin of Earthquake Engineering. 2018;16(10):4497-4514. https://doi.org/10.1007/s10518-018-0317-9
[27] Tatsuoka F, Zhou S, Sato T, Shibuya S. Method of evaluating liquefaction potential and its application. Report on Seismic Hazards in the Soil Deposits in Urban Areas, Ministry of Education of Japan, 75-109, 1990 (in Japanese).